FROM PUBLICLY AVAILABLE WEBCAMS TO ICE-AVALANCHE HAZARD ASSESSMENT: A DECADE OF SERAC FALLS FROM A HANGING GLACIER OF THE MONT-BLANC MASSIF (FRANCE)

Grégoire Guillet[*1,2], Ludovic Ravanel[3,1]

[1]*Avalanche Research Program, Simon Fraser University, Burnaby, BC, Canada*
[2]*Department of Geosciences, University of Oslo, Oslo, Norway*
[3]*EDYTEM, University Savoie Mont-Blanc, CNRS (UMR 5204), Le Bourget du Lac, France*

ABSTRACT: Outside a few studies of ice masses threatening valleys (*e.g.*, Weissmies, Taconnaz, and Grandes Jorasses in the Alps), hanging glaciers (HGs) and their dynamics remain poorly understood. Because individual collapses are rarely observed and measured, the size and frequency of serac falls remain largely unquantified. We use the Contamine-Négri HG, on the north-eastern side of Mont Blanc du Tacul (4248 m a.s.l., Mont-Blanc massif, France), as a case study. Repeated serac falls from this HG trigger ice avalanches across heavily travelled mountaineering routes. Recent near-fatal events include 22 May 2020, when $\sim$15,000 m^3 of ice partially rebounded nearly 50 m up the north face of Pointe Lachenal, and 8 May 2025, when $>$60,000 m^3 generated two avalanches (450 m northwards, burying three people, and 700 m eastwards). We analyzed a decade (2016–2026) of daily imagery from two webcams successively installed at the Aiguille du Midi (3842 m a.s.l.), 1.7 km from the HG. Using single-image photogrammetry with a Bayesian model, we estimated the volume of each major collapse. For every resolvable event, we measured the released ice surface area and volume, building a decade-long catalogue and magnitude-frequency distribution. Repurposing publicly available webcam archives as calibrated, georeferenced measurements transforms tourism infrastructure into a quantitative tool for studying serac falls and ice avalanches. The resulting magnitude-frequency distribution and seasonal release rates provide return periods and time-varying exposure probabilities, supporting seasonal guidance and future assessment of climate-driven changes. Peak activity coincides with route use, mainly from late spring to late autumn.

KEYWORDS: Ice avalanches, serac falls, hanging glacier, Bayesian inference, Mont Blanc du Tacul.

1. INTRODUCTION

Hanging glaciers (HGs) are cold (negative temperatures) and steep glaciers located on a mountain slope, commonly perched above a cirque or valley glacier. HGs are among the most spectacular and potentially hazardous components of high-Alpine environments. Their steep geometry and the limited basal support of their front favor recurrent ice break-offs, ranging from small serac falls to occasionally catastrophic collapses involving hundreds of thousands or even millions of cubic meters of ice. Although the consequences are generally confined to high-elevation areas and mountaineering routes, some ice avalanches can travel several kilometers and reach inhabited valleys, as documented for the Altels, Weisshorn, Taconnaz and Grandes Jorasses glaciers in the European Alps (Pralong and Funk 2006; Faillettaz et al. 2011; Vincent et al. 2015; Margreth et al. 2011).

The physical processes governing HGs' instability have been investigated through field observations, photogrammetry, numerical modelling and seismic monitoring. Different failure mechanisms have been identified, depending on glacier geometry, thermal regime, basal conditions and the progressive accumulation of damage. In cold hanging glaciers, increasing gravitational stress and internal fracture can produce a progressive acceleration towards failure, sometimes accompanied by characteristic changes in surface velocity (Pralong and Funk 2006). However, these observations also demonstrate the fundamental difficulty of predicting the exact timing and magnitude of individual break-offs. Geometrical thresholds may indicate a potentially unstable configuration, but they are neither necessary nor sufficient to determine when a collapse will occur (Vincent et al. 2015).

Consequently, a complementary approach is to characterize ice-avalanche activity statistically rather than attempting to predict individual failures. Long-term observations of the Taconnaz hanging glacier demonstrated that repeated photogrammetric measurements can quantify both the volume and frequency of major collapses, providing information on the magnitude-frequency characteristics of ice avalanches (Vincent et al. 2015). Similar monitoring at the Whymper glacier of the Grandes Jorasses has shown how systematic observations can support hazard assessment and operational safety strategies (Margreth et al. 2011; Faillettaz et al. 2016).

* *Corresponding author address:*
Grégoire Guillet, Department of Geosciences, Faculty of Mathematics and Natural Sciences, University of Oslo, Oslo, Norway
email: gregoire.guillet@geo.uio.no

https://doi.org/10.15788/1790099244

Despite these advances, hanging glaciers remain comparatively poorly documented, particularly with respect to the full spectrum of serac-fall sizes and frequencies. This limitation is partly methodological: large collapses are infrequent, access to unstable glacier fronts is difficult and conventional monitoring programs are costly. Recent work on the Mallory HG (Mont-Blanc massif) illustrates the value of combining morphological, thermal and dynamic observations to characterize the evolution of such systems (Cailhol et al. 2026). Yet, continuous observations capable of establishing a decade-scale catalogue of individual ice-avalanche events remain rare.

Here, we investigate the Contamine-Négri HG (CN HG) on the north-eastern side of Mont Blanc du Tacul (Mont-Blanc massif, France). The HG repeatedly generates serac falls that feed ice avalanches crossing frequently used mountaineering routes. We reconstruct its recent collapse activity using a decade of daily webcam imagery and single-image photogrammetry. Our objectives are (1) to establish a comprehensive catalogue of major ice-fall events, (2) to quantify their released volumes and frequencies, (3) to derive the magnitude-frequency distribution of ice avalanches, and (4) to examine their seasonal variability in relation to human exposure. By transforming publicly available imagery collected for tourism into calibrated, georeferenced measurements, we provide a cost-effective framework for quantifying serac-fall activity and developing a statistical basis for hazard assessment in rapidly changing high-Alpine environments.

2. STUDY SITE

2.1. The Contamine-Négri hanging glacier

The Contamine-Négri HG (CN HG) is located on the north-eastern side of Mont Blanc du Tacul (4248 m a.s.l., Mont-Blanc massif, French Alps; Figure 1). The glacier occupies a steep, north-east-facing slope above the Géant glacier in the upper Mer de Glace basin (largest glacier in the French Alps). Its elevated position and steep morphology give it the characteristic configuration of a HG: the cold ice body, frozen to the permafrost (Magnin et al. 2015), is perched above the surrounding cirque glacier and terminates in a steep front from which recurrent serac falls occur.

The CN HG extends approximately 315 m horizontally and over a vertical elevation difference of about 340 m. It covers an area of about 40,000 m^2. Its front is located at approximately 3760 m a.s.l. and it is approximately 170 m wide and more than 40 m thick. The glacier has undergone substantial morphological changes during the last decades (Figure 1). In particular, historical imagery reveals the progressive and almost complete disappearance of an ice connection along its left margin with the Géant glacier. This progressive decoupling has contributed to the development of a distinct and steeply inclined ice body.

The HG is situated in a highly frequented mountaineering area. Several classic climbs, mountaineering and ski routes cross or pass beneath the potential trajectory of released ice avalanches, making the site particularly relevant for hazard assessment. Serac falls from the CN HG have repeatedly produced ice avalanches that propagate over the surrounding slopes and routes. The magnitude of these events can vary considerably, from relatively small ice falls to collapses involving tens of thousands of cubic meters of ice.

3. DATA AND METHODS

3.1. Data

The primary data are oblique images of the Mont Blanc du Tacul north face from a fixed tourism panorama webcam at the Aiguille du Midi (3842 m a.s.l.), installed by the *Compagnie du Mont-Blanc* which operates the Aiguille du Midi cable-car, for visitor views and not for glacier monitoring. It images the CN HG and the Pointe Lachenal descent from about 1.7 km away. We repurpose its public archive as a decade-long monitoring record. Images span 2016 to 2026 at roughly daily cadence. The camera was replaced several times over that period, producing distinct resolution eras, so we take one era as the reference and co-register the others to it, giving a single image geometry across the record.

Terrain data are a 0.5 m LiDAR DEM (IGN 2021 LiDAR HD, Lambert-93, EPSG:2154), used as the reference inverse perspective surface for monoplotting and as the current surface for elevation change, and a 4 m DEM from the *Régie de Gestion des Données des Pays de Savoie* (Lambert-93), built from 1998 aerial photographs and revised through 2010, with a reported vertical RMSE of 1 m in flat terrain rising to 4 m in steep Alpine terrain (Guillet et al. 2020). The older DEM predates the recent thinning and is used only to estimate serac fall volume. Camera calibration rests on 11 control points identified on stable rock around the glacier.

Figure 1: The Contamine-Négri hanging glacier (CN HG) on the north-eastern side of Mont Blanc du Tacul (4248 m a.s.l., Mont-Blanc massif, France) in the early 2000s (left) and in July 2026 (right). Note the significant retreat of the front on the right bank.

3.2. From pixels to meters: Monoplotting

We recover map coordinates from single oblique images using probabilistic monoplotting (Guillet et al. 2020; Guillet and Ravanel 2020) as it is the relevant choice for a fixed, non-metric webcam. The camera model combines a calibrated interior model with an exterior orientation and is estimated through Bayesian inference. After recovering the camera parameters (location and optical parameters), each traced image feature is projected onto the high-resolution LiDAR DEM by inverse perspective. This places any outline drawn on an image into three-dimensional terrain coordinates without stereo or repeat photogrammetry. Post-2021 frames, recorded at a different resolution, are first warped onto the reference image grid so a single geometry applies across the whole record. Each deprojection retains an ensemble of likely camera parameters estimated through Markov Chain Monte Carlo and thus carries a positional uncertainty onto the deprojected deposit outlines used for runout.

3.3. Collapse catalogue

A single operator identified 45 front-collapse events across the record (July 2016 to September 2025) and, for each event, traced the front outline of the glacier before and after the collapse and, where debris were visible, the deposit footprint. The collapse scar is the front-retreat area between the bracketing frames, summed only over sectors where the terminus retreated so that simultaneous advance elsewhere cannot offset it, and converted to ground units with the cliff ground scale (1.74 m^2 per pixel). Volume is obtained by multiplying the surface by a 40 m glacier thickness, taken as the median difference between the older 4 m DEM and the current LiDAR DEM over the serac zone. The spatial spread of that difference ($\pm$22 m) is the dominant volume uncertainty and is carried as a per-event error bar. Because one thickness is applied to every event, this uncertainty is a common scale that shifts the absolute volumes by about 54 % but leaves the distribution shape and the event ranking intact. Of the 45 events, 40 with a resolvable retreat scar were sized, and 17 left webcam-visible debris that could be traced downslope. Small and winter events rarely leave a mappable footprint and set the completeness floor of the catalogue. Because imaging gaps are uneven, event rates are corrected for observation effort, the fraction of days carrying a usable image, rather than reported as raw counts.

3.4. Runout mapping

For each of the 17 traced deposits, we form the swept wedge between the release front and the convex hull of the deposit, and stack the wedges into a cumulative reach field, defined at each cell as the fraction of mapped avalanches reaching it. We clip the field to physically reachable terrain with an energy-line criterion (minimum travel angle 24°) and a slope threshold (below 43°), which removes over-ridge and steep-rock cells.

3.5. Route exposure

To relate the hazard to human presence (alpinists), we overlay travel paths on the reach field, following the track-based route-risk approach used for backcountry skiing (Schmudlach 2024) and the encounter-probability framework of transportation avalanche risk (Wilhelm 1998). Paths were hand-digitized from observed usage and registered to the DEM. For each path, we report the length-weighted mean reach probability and the exposed fraction, the share of the route in cells with reach probability above 0.05. Because we digitize route presence rather than calibrated user counts, we report individual per-crossing risk rather than collective risk, estimating the expected number of encounters μ and the probability of being caught P_{c} as

$$\mu = \lambda\, t\, \bar{p}, \qquad P_{\mathsf{c}} = 1 - e^{-\mu}, \tag{1}$$

where λ is the event rate, t the exposure time and $\bar{p}$ the mean reach probability along the route. Crossing time is taken as 10 to 20 minutes and the conditional fatality factor as 0.5.

4. RESULTS AND DISCUSSION

4.1. Serac-fall dynamics at the Contamine-Négri hanging glacier

The size distribution of the 40 serac falls is heavy-tailed (Figure 2). Volumes span more than two orders of magnitude, with a median of 13,000 m^3, a mean of 15,500 m^3 and a maximum of 68,000 m^3. Small and medium events dominate the count with large and major events forming the heavy tail. We test the tail of the event size distribution for a power law following the maximum-likelihood method of Clauset et al. (2009). It fits the lower bound and exponent by maximum likelihood, then compares the power law against a lognormal by a likelihood-ratio test. The fitted power-law exponent is 2.58. That is comparable to, and at the upper end of, values for snow-slab avalanches (2.2 $\pm$ 0.1; Faillettaz et al. 2004) and tidewater-glacier calving (1.7 to 2.0; Chapuis and Tetzlaff 2014). A power law is the expected form, because calving termini behave as self-organized critical systems (Åström et al. 2014). At n = 40, however, the power law and the lognormal cannot be told apart. We therefore report the tail as heavy, and as consistent with but not diagnostic of a self-organized critical system. The uncertainty in glacier front thickness shifts the absolute volumes but leaves the distribution shape and the event ranking unchanged. Small and winter events below the mapping threshold are undercounted, so the low-magnitude end is truncated, while the upper tail is more completely sampled. A heavy-tailed hazard of this kind is managed through rate, seasonality and exposure rather than by predicting individual events, unless the front leaves a monitorable precursor.

Size is only one dimension of the hazard, as ice avalanche timing matters just as much. We measure the waiting times between falls, dropping any interval that spans a long (typically longer than 2 weeks) imaging gap, so unseen events cannot inflate the distribution. The median recurrence time is 23 days. The distribution is strongly over-dispersed relative to a random-in-time process, with a coefficient of variation of 1.45, against 1.0 for a standard Poisson process. This over-dispersion is not peculiar to our site. Iceberg calving at tidewater glaciers shows the same pattern, with coefficients of variation of 1.5 to 1.9 and intervals that are neither exponential nor power-law (Chapuis and Tetzlaff 2014). The falls also carry no memory of their size. Indeed, serac-fall volume is uncorrelated with the preceding or the following interval (Spearman rho of 0.07 and 0.20, n = 32). There is no load-and-release cycle, in which a large fall would follow a long quiescence period. Over-dispersion without memory is consistent with a rate driven by external forcing rather than by internal stick-slip triggering.

Serac falls concentrate in June and July with summer rates being several times winter rates, even after correcting for uneven imaging (Figure 3). Over the decade, that concentration has sharpened and the overall rate has risen. We split the record into two halves of equal observed length. The first (2016 to 2021) holds 16 events. The second (2021 to 2025) holds 29. The melt-season share rose from 69 to 90 %. July events more than doubled, with winter tails nearly vanishing. Corrected for image availability, the summer rate is 2.4 times higher in the second half, from 5.9 to 14.2 events per summer. We further consider this ratio to be conservative, as potentially uncounted small and winter events are most likely missed in the 2016–2021, colder part of the record. These results further match the known sensitivity of steep Alpine glaciers and their seracs to atmospheric warming (Faillettaz et al. 2015). We establish this pattern, but we do not attribute it to a measured forcing, which would need the catalogue coupled to local temperature or melt records.

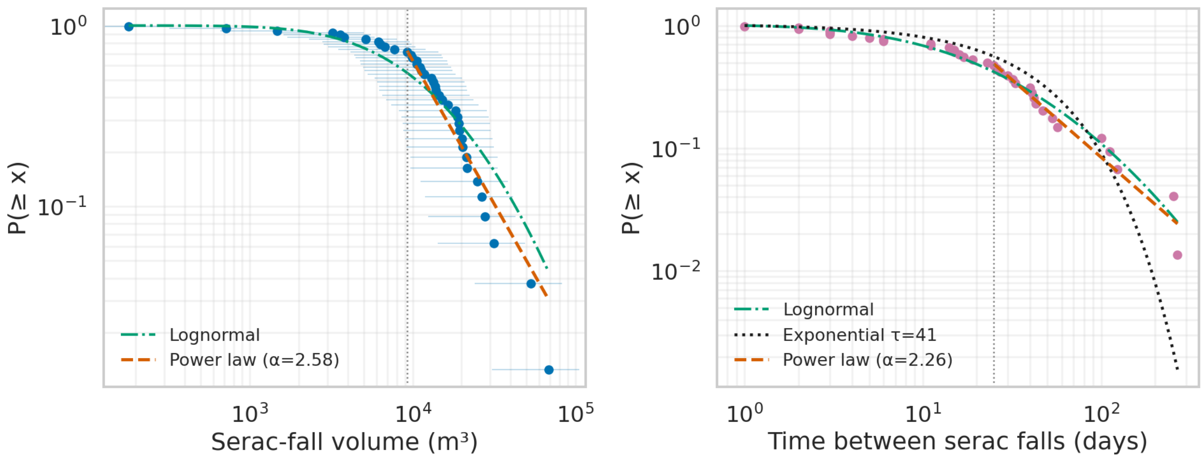

Figure 2: Complementary cumulative distributions of serac-fall volume (left) and inter-event waiting time (right), with maximum-likelihood fits. Volume (n = 40) is fit equally well by a lognormal and a tail power law (α = 2.58, above x_min at the dotted line). Waiting time (n = 37, imaging-gap intervals removed) is over-dispersed, best fit by a lognormal and worst by an exponential (τ = 41 d). Horizontal bars on the volume panel are the $\pm$54 % thickness uncertainty. Axes logarithmic.

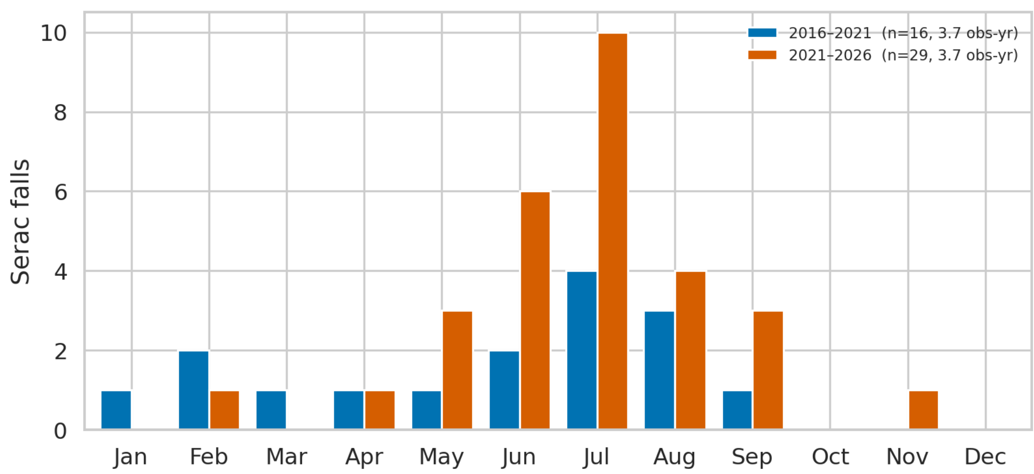

Figure 3: Monthly serac-fall counts for two eras of equal observed duration ($\sim$3.7 observation-years each after imaging-gap removal), so counts compare directly as rates. Blue, 2016–2021 (n = 16); vermilion, 2021–2025 (n = 29). Activity peaks in June–July and, in the recent era, is both higher and more sharply seasonal.

4.2. Ice avalanche runout and route exposure

Of the 40 serac falls, only 17 left debris we could trace. The rest deposited beyond the Lachenal ridge, out of the camera's view. That also makes the mapped reach a lower bound on the far side. The 17 traceable deposits have short, steep travel angles, 25 to 41°, mean 34°. That is well above the 17 to 22° of large, mobile ice avalanches (Alean 1985). They stop close below the release, over a drop of about 200 m, from 3740 m a.s.l. to toes at 3510 to 3610 m. They do not run far downslope. We stack the traced deposits into a swept-wedge field, and clip it to terrain reachable under an energy-line and slope criterion. The result is a cumulative reach probability that overlaps the descent from the Aiguille du Midi ridge to Pointe Lachenal (Figure 4). The mapped field is built from ice deposits alone. On one winter occasion, a small serac fall remotely triggered a much larger dry-slab avalanche. The field is therefore a lower bound on total avalanche hazard, and not only on far-side ice reach. The coupling is also undersampled, since a triggerable snowpack is present in the season where our catalogue is least complete.

Laying the paths over that field shows that the busiest line is also the most exposed. The main descent runs 480 m through the fall zone. Along that length, 64 % lies in cells reached by at least

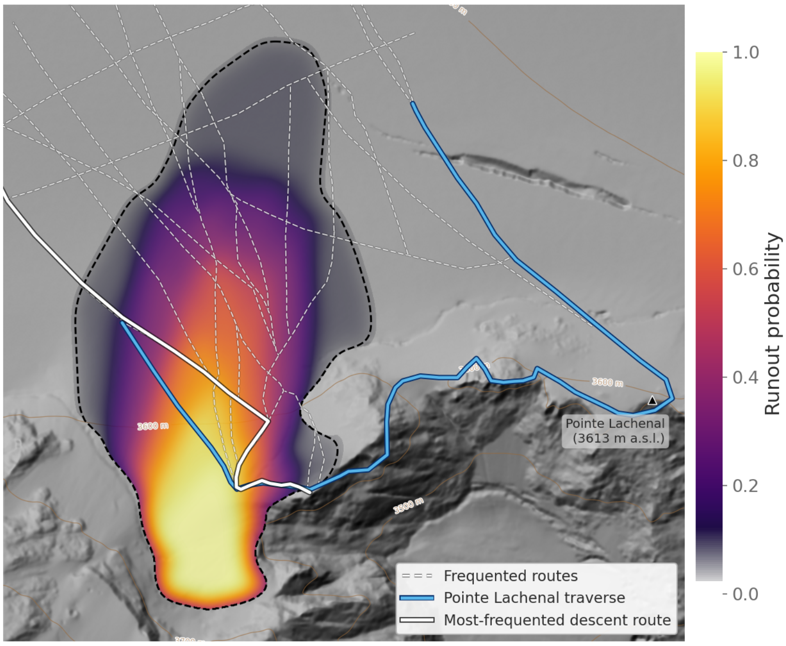

Figure 4: Ice-avalanche runout reach probability (fraction of the 17 mapped deposits reaching each cell) over a LiDAR hillshade with 100 m contours, at the Contamine-Négri hanging glacier. Observed travel routes overlaid: white dashed, frequented network; blue, Pointe Lachenal traverse; solid white, most-frequented descent, which crosses the high-probability core. Dashed black line, maximum mapped extent; triangle, Pointe Lachenal summit (3613 m a.s.l.).

one fall in twenty, the mean reach probability is 0.35, and the peak is 0.91 in the core. Across the whole 8 km network, only 36 % of travelled length is exposed. The main descent is thus exposed along about twice the network-average fraction. This overlap is fixed in space, but the hazard is not. The per-crossing chance of an encounter scales with the fall rate, which has risen 2.4-fold. The traffic is rising too. The Pointe Lachenal traverse has become a de-facto fallback for parties leaving the classic Arête des Cosmiques, whose rock has grown less reliable under recent heatwaves and warming-driven rockfall (Ravanel et al. 2017; Mourey et al. 2022). It also offers an accessible introductory glacier route. The shift is sharpest among guided parties, whose itineraries increasingly reflect these climate-driven hazards (Cailhol et al. 2025). More falls above and more people below are two climate-driven trends that compound one another.

Turning exposure into risk needs the standard units of quantitative risk assessment. It also needs a split between the recreational party and the professional guide, who accumulate exposure very differently. Combining the summer event rate (about 0.12 per day), a crossing time of 15 minutes, the mean reach probability of 0.35 and a fatality fraction of 0.5, a single summer crossing of the main descent carries a fatality risk of about 2×10^{-4}, some two hundred micromorts, where one micromort is a one-in-a-million chance of death (Howard 1989). A skydive is about 8 micromorts and a full day of alpine mountaineering is of order 10^2 micromorts (Weinbruch and Nordby 2013), so one crossing carries risk of the same order as a whole alpine day, concentrated into the few minutes beneath the serac. The figure is uncertain by a factor of a few, through the event rate, the exposure time and the assumed fatality fraction. The trend is firmer. With the summer rate up 2.4-fold, a crossing today carries about 2.4 times the risk of a decade ago.

For a guide, the same per-crossing risk becomes an occupational one. A guide crosses the zone around five times a season, which brings the annual risk from this single hazard to about 1×10^{-3} per year. That is roughly a third of a guide's all-cause mountain fatality risk of about 3×10^{-3} per year (about 121 French guides died in mountain incidents between 1995 and 2018, among some 1,300 to 1,600 active guides). One glacier on one route therefore accounts for a substantial share of a guide's total mountain risk. Because even a small fall is lethal, this risk scales with how often a guide is beneath the serac, not with the size of the worst event. A serac fall here cannot be seen coming or outrun. The only controls are route choice and timing, above all avoiding the melt-season and midday windows when the rate peaks.

5. CONCLUSIONS AND OUTLOOKS

In this study, we repurpose tourism webcams, through probabilistic monoplotting and inverse perspective, to compile a 10-year catalogue of 45 serac falls at the Contamine-Négri hanging glacier. We find that the serac-fall rate has increased by a factor of 2.4 and become more strongly concentrated in the melt season. We also find that the most frequented descent route is the most exposed to serac-fall runout, so hazard frequency and route use are increasing concurrently.

Our analysis has several limitations. The runout and exposure estimates rest on a single fixed camera pose and on near-side deposits, and the risk estimates are order-of-magnitude. The far-side reach and the decadal trend are both conservative. Against these limitations, the approach is low-cost, retrospective and transferable, as many HG already lie within the field of view of an existing tourism or infrastructure camera.

The record also indicates a path toward forecasting rather than hindsight alone. We observe that the pre-failure protrusion of the calving front appears to correlate with the volume of the subsequent fall. This geometric precursor could be monitored operationally with a fixed camera, and it bears on the question of predictability raised above. We report it as a direction for further work rather than a validated result. The camera's field of view also includes the lower Trois Monts route, the second most frequented ascent of Mont Blanc and a recurrent site of fatal avalanches. We are extending the analysis to that route.

ACKNOWLEDGEMENTS

The authors would like to thank the *Compagnie du Mont-Blanc* for facilitating access to the site and for allowing them to use the webcam images.

REFERENCES

Alean, J. (1985). Ice avalanches: some empirical information about their formation and reach. In: Journal of Glaciology 31.109, pp. 324–333. https://doi.org/10.3189/S0022143000006419.

Åström, J. A., Vallot, D., Schäfer, M., Welty, E. Z., O'Neel, S., Bartholomaus, T. C., Liu, Y., Riikilä, T. I., Zwinger, T., Timonen, J., and Moore, J. C. (2014). Termini of calving glaciers as self-organized critical systems. In: Nature Geoscience 7, pp. 874–878. https://doi.org/10.1038/ngeo2290.

Cailhol, X., Ravanel, L., and Mourey, J. (2025). Mapping climate-change-related processes affecting most frequented routes by French mountain guides. In: Geographica Helvetica 80, pp. 527–544. https://doi.org/10.5194/gh-80-527-2025.

Cailhol, X., Ravanel, L., Robson, B., Malet, E., Mourey, J., Bazin, J., and Magnin, F. (2026). Assessing the evolution of hanging glacier: multi-method monitoring of the Mallory glacier (Mont-Blanc massif, France). In: Geografiska Annaler: Series A, Physical Geography 108.1, pp. 1–21. https://doi.org/10.1080/04353676.2026.2688689.

Chapuis, A. and Tetzlaff, T. (2014). The variability of tidewater-glacier calving: origin of event-size and interval distributions. In: Journal of Glaciology 60.222, pp. 622–634. https://doi.org/10.3189/2014JoG13J249.

Clauset, A., Shalizi, C. R., and Newman, M. E. J. (2009). Power-law distributions in empirical data. In: SIAM Review 51.4, pp. 661–703. https://doi.org/10.1137/070710111.

Faillettaz, J., Funk, M., and Vagliasindi, M. (2016). Time forecast of a break-off event from a hanging glacier. In: The Cryosphere 10, pp. 1191–1200. https://doi.org/10.5194/tc-10-1191-2016.

Faillettaz, J., Funk, M., and Vincent, C. (2015). Avalanching glacier instabilities: review on processes and early warning perspectives. In: Reviews of Geophysics 53.2, pp. 203–224. https://doi.org/10.1002/2014RG000466.

Faillettaz, J., Louchet, F., and Grasso, J.-R. (2004). Two-threshold model for scaling laws of noninteracting snow avalanches. In: Physical Review Letters 93.20, p. 208001. https://doi.org/10.1103/PhysRevLett.93.208001.

Faillettaz, J., Sornette, D., and Funk, M. (2011). Numerical modeling of a gravity-driven instability of a cold hanging glacier: reanalysis of the 1895 break-off of Altelsgletscher, Switzerland. In: Journal of Glaciology 57.205, pp. 817–831. https://doi.org/10.3189/002214311798043852.

Guillet, G., Guillet, T., and Ravanel, L. (2020). Camera orientation, calibration and inverse perspective with uncertainties: a Bayesian method applied to area estimation from diverse photographs. In: ISPRS Journal of Photogrammetry and Remote Sensing 159, pp. 237–255. https://doi.org/10.1016/j.isprsjprs.2019.11.007.

Guillet, G. and Ravanel, L. (2020). Variations in surface area of six ice aprons in the Mont-Blanc massif since the Little Ice Age. In: Journal of Glaciology 66.259, pp. 777–789. https://doi.org/10.1017/jog.2020.46.

Howard, R. A. (1989). Microrisks for medical decision analysis. In: International Journal of Technology Assessment in Health Care 5.3, pp. 357–370. https://doi.org/10.1017/S0266462300007443.

Magnin, F., Brenning, A., Bodin, X., Deline, P., and Ravanel, L. (2015). Statistical modelling of rock wall permafrost distribution: application to the Mont Blanc massif. In: Géomorphologie 21.2, pp. 145–162. https://doi.org/10.4000/geomorphologie.10965.

Margreth, S., Faillettaz, J., Funk, M., Vagliasindi, M., Diotri, F., and Broccolato, M. (2011). Safety concept for hazards caused by ice avalanches from the Whymper hanging glacier in the Mont Blanc Massif. In: Cold Regions Science and Technology 69.2–3, pp. 194–201. https://doi.org/10.1016/j.coldregions.2011.03.006.

Mourey, J., Lacroix, P., Duvillard, P.-A., Marsy, G., Marcer, M., Malet, E., and Ravanel, L. (2022). Multi-method monitoring of rockfall activity along the classic route up Mont Blanc (4809 m a.s.l.) to encourage adaptation by mountaineers. In: Natural Hazards and Earth System Sciences 22, pp. 445–460. https://doi.org/10.5194/nhess-22-445-2022.

Pralong, A. and Funk, M. (2006). On the instability of avalanching glaciers. In: Journal of Glaciology 52.176, pp. 31–48. https://doi.org/10.3189/172756506781828980.

Ravanel, L., Magnin, F., and Deline, P. (2017). Impacts of the 2003 and 2015 summer heatwaves on permafrost-affected rock-walls in the Mont Blanc massif. In: Science of the Total Environment 609, pp. 132–143. https://doi.org/10.1016/j.scitotenv.2017.07.055.

Schmudlach, G. (2024). A routing algorithm for backcountry ski tours. In: Proceedings of the International Snow Science Workshop (ISSW). Tromsø, Norway.

Vincent, C., Thibert, E., Harter, M., Soruco, A., and Gilbert, A. (2015). Volume and frequency of ice avalanches from Taconnaz hanging glacier, French Alps. In: Annals of Glaciology 56.70, pp. 17–25. https://doi.org/10.3189/2015AoG70A017.

Weinbruch, S. and Nordby, K.-C. (2013). Fatalities in high altitude mountaineering: a review of quantitative risk estimates. In: High Altitude Medicine & Biology 14.4, pp. 346–359. https://doi.org/10.1089/ham.2013.1046.

Wilhelm, C. (1998). Quantitative risk analysis for evaluation of avalanche protection projects. In: 25 Years of Snow Avalanche Research. Ed. by Hestnes, E. NGI Publication 203. Oslo: Norwegian Geotechnical Institute, pp. 288–293.